LANGMUIR

Hysteretic Behavior of Capillary Bridges between Flat Plates

Moyosore S. Odunsi, Jeffrey F. Morris, and Mark D. Shattuck*

Read Online

ACCESS | Metrics & More | Article Recommendations

ABSTRACT: We studied the evolution of capillary bridges between nominally flat plates undergoing multiple cycles of compression and stretching in experiments and simulations. We varied the distance between the plates in small increments to study the full evolution of the bridge shape. Experiments show that contact angle hysteresis determines the shape of the bridge. In sliding drops, hysteresis can be modeled using a contact angle-dependent resistive force $\tilde{F}_R$ applied at the contact line. We developed a model that accurately captures the evolution of the bridge shape by combining $\tilde{F}_R$ and constrained energy minimization. Unlike previous work, this allows for both complete and partial contact line pinning. We also explored the effect of using nonparallel plates. The asymmetry in the bridge shape causes the movement of the center of mass of the bridge and can be explained by contact angle hysteresis. We find that even a slight misalignment between the flat plates can have a measurable effect.
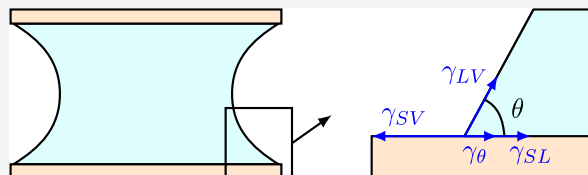
1. INTRODUCTION

Capillary bridges are a prominent part of many systems, such as water saturation in soil,[1] inkjet printing,[2] and the feeding of shorebirds.[3] In addition, humidity can cause water capillary bridges to form between atomic force microscopy probes and samples.[4] This has been shown to impact the force measurements. Studying the behavior and, in particular, the forces associated with these bridges is a necessary part of understanding any system where bridges occur.

The equilibrium contact angle that the bridge makes with an ideal surface can be found through a force balance at the contact line using by Young's equation.[5] This equation allows for one equilibrium contact angle, θ_0. In reality, capillary bridges will exhibit a range of different contact angles for a given volume and height. This phenomenon is called contact angle hysteresis. It can be understood in terms of energy minimization. There is an absolute (or global) Gibbs energy minimum that corresponds with Young's formulation of contact angles, but there is also an array of local energy minima that each correspond to different contact angles.[6−8] Surface roughness, chemical heterogeneity on the solid surface, and films on the solid caused by solutes in the liquid are all possible causes of contact angle hysteresis.[9] There has been research on dynamic contact angle hysteresis in capillary bridges. There is greater contact angle and normal force hysteresis with faster contact line movement.[10] This paper will not look at dynamic conditions, but instead focus on scenarios where the bridge hysteresis can be studied under static conditions, i.e., low Ca and low Re situations.[11,12]

Contact angle hysteresis is thus an important factor in the shape of and forces associated with capillary bridges. Under conditions of varying bridge height, previous researchers have

made a distinction between r-bridges, with a fixed bridge radius and changing θ, and θ-bridges, where there is a fixed θ and changing bridge radius.[13,14] According to these models, when the bridge height is increased, the bridge radius stays constant until the contact angle reaches its advancing value, θ_a, and when the bridge height is decreased, the bridge radius stays constant until the contact angle reaches its receding value, θ_r. After reaching the advancing and receding contact angles, the bridge will stay at a constant contact angle while the contact radius either advances onto the solid surface or recedes back in the direction coated by liquid. This creates a limiting range for the contact angles, $\theta_r \leq \theta \leq \theta_a$. The equilibrium contact angle is typically between the advancing and the receding contact angles. The distinction between changing θ and changing radius has guided models for capillary bridge hysteresis under static conditions that use computational techniques to calculate the bridge shape.[14−16] Such models do not allow for the possibility of partial contact line pinning.

The tangential forces associated with contact line pinning have also received attention for many years. In 1925, Adam and Jessop introduced a "line tension" that acted like friction to prevent contact line motion.[17] This force was the unbalanced contact line force per unit length that arose from a contact angle different from Young's equilibrium contact angle. Researchers have adapted this idea to model shearing bridges
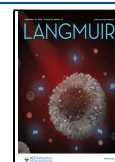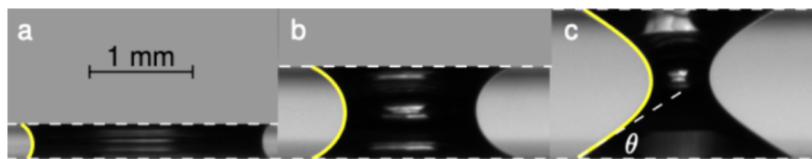
Figure 1. Experimental images for three different bridge heights. The bridge outlines are found through MATLAB image processing. (a) The bridge is at its minimum height; the contact radius and angle are both at their largest values. (b) The bridge is at an intermediate height. (c) The bridge is at its maximum height; the contact radius and angle are both at their minimum values.

between flat plates using multibody dissipative particle dynamics simulations,[18] surface energy minimization,[19] lattice Boltzmann simulations,[20] and experiments.[19,21] Similarly, it has successfully been used to model the tangential force arising from sliding drops.[22−26] In both cases, the advancing and receding contact angles have been included in the tangential force equations. However, there is still a need to investigate the link between contact angle hysteresis and tangential forces for capillary bridges with changing heights. These bridges are unique because the tangential contact-line force sums to zero for the circularly symmetric case, making it difficult to measure.

Contact angle hysteresis for bridges between nonparallel plates can cause motion of the bridge toward the point where the surfaces would meet if extended sufficiently far.[3,27] This motion occurs when either the angle or the height between the surfaces is changed. Under certain circumstances, these two scenarios are equivalent.[28] The asymmetry of the bridge means that the advancing and receding angles are reached by different parts of the bridge at different times. In particular, when the angle or height between the surfaces decreases, the contact angles on the narrower side of the bridge will reach the advancing angle first which causes net movement toward the narrow side. Likewise, when the angle or height is increased, the contact angles on the wider side of the bridge will reach the receding value first, which again causes net movement toward the narrow side.

This paper presents an experimental analysis of hysteretic capillary bridges undergoing stretching and compressing coupled with a new model for simulating these bridges by introducing a "resistive force" that resists contact line movement. This model applies to bridges between parallel and nonparallel flat plates. We first develop the capillary bridge concepts to establish the context of our work and then describe the experimental procedure and results. Finally, the theoretical model is developed and compared with experimental results.

2. EXPERIMENTAL PROCEDURE

Two identical borosilicate glass coverslips (Fisher Scientific, 22 mm × 22 mm, no. 2) are used as the solid surfaces. The top surface is attached to a Stable Microsystems Texture Analyzer, which moves in the vertical direction in 2 μm increments. This allows for the study of small changes in the bridge height. The bottom surface is attached to an analytical balance (Radwag AS 82/220.R2) and kept stationary throughout the experiment. The analytical balance can measure forces to ±0.1 μN accuracy. At the beginning of each experiment, we placed a microliter scale droplet of glycerin (Fisher Scientific, ACS grade) on the bottom surface. The balance is zeroed to subtract the weight of the droplet. The top surface is lowered onto the droplet, and a capillary bridge is formed. After every change in bridge height, there is a 15 s wait. After this time, there is no noticeable change in the bridge structure, and thus, a steady state has been reached; at this time, normal force measurements and images of the bridge are taken.

The bridge height was lowered from a maximum height of 0.53 mm to a minimum height of 0.33 mm and then raised back to the maximum height three times in succession. The small capillary

number, Ca $\sim O(10^{-6})$, and Bond number, Bo $\sim O(10^{-2})$, justify treating viscosity and gravity as negligible. The top glass surface is tilted at most by a small angle ($<1°$).

A digital camera (Basler A102f) with a macro lens captures images of the bridge shape. Example images are shown in Figure 1 for the three bridge heights. An additional camera looks down through the top surface and images the top contact line. Image processing is done through Matlab. The contours of the bridge are found through a convolution procedure and then fitted to a third-degree polynomial. The contact angles between the flat plates and the bridge are calculated from the image data. The radius is half the distance between the two top or two bottom edges of the bridge. The center of the bridge is the halfway point between these edges. The drift is the distance that the edges of the bridges move from their starting points at the beginning of the experiment.

3. RESULTS

3.1. Experimental Results. Figure 2 shows the evolution of a ~ 1 μL capillary bridge. The bridge height was lowered and then raised three consecutive times as represented by the three lines on the plots. The arrows follow the progression of the
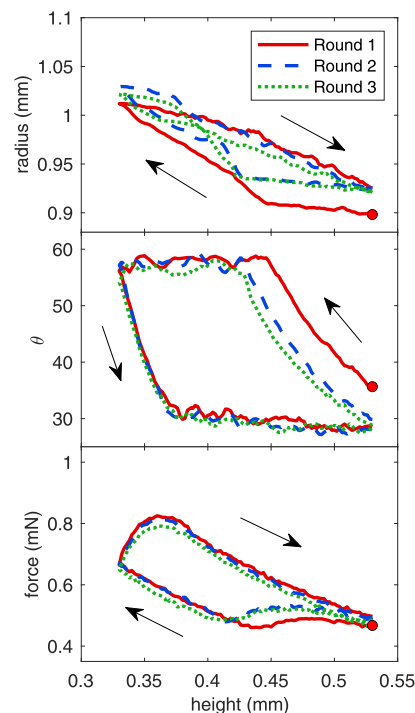
Figure 2. Experimental results for a capillary bridge between two flat plates over multiple cycles. The bridge height is lowered from 0.53 to 0.33 mm and then raised back to the original height three times. The arrows follow the evolution of the contact radius, contact angle, and normal force under changing bridge height. Positive normal force indicates attraction between the plates. The dot marks the beginning of the process.

contact radius, angle and normal force. Data for the top left contact angle and radius are shown, but all the angles and radii displayed similar behavior.

The solid line represents the first experimental cycle. The initial conditions were $H = 0.53$ mm and $\theta = 36°$. This was between the advancing and receding contact angle values so the contact line was unable to move freely on the solid surface, and lowering the bridge height only caused a small change in the contact radius. After the contact angle reached $\theta_a = 58°$, the contact line depinned and the contact radius advanced more rapidly with the decrease in bridge height. At $H = 0.33$ mm, the direction of motion was reversed and the plates were separated, i.e., the height was increased. The stretching stage did not show the sharp transition to a limiting angle that the compressing stage displayed, but once the contact angle reached $\theta_r = 29°$, the contact angle decreased at a much slower rate. At the onset of stretching of the bridge, there was an immediate decrease in the contact radius.

For the first cycle of the experiment, the initial bridge shape is different than that for the next two cycles. This is a result of hysteresis: without it, the bridge properties at a given height would always be the same. One consequence of the hysteretic behavior is that the work done by compressing and stretching the bridge is not always the same magnitude. The work done on the system by changing the bridge height is found by integrating the normal force across all bridge heights. For this experiment, the net work done during the first, second, and third cycles are 29.4, 23.7, and 23.5 nJ, respectively. The work done within the second and third cycles is the same within the margin of error. The work for the first cycle is higher than for the next two cycles as would be expected from the force curves in Figure 2.

The angle and radius data in Figure 2 show behavior similar to that found in previous experiments with two key differences. Previously reported contact angle and radius hysteresis experiments have found total contact line pinning until the advancing and receding contact angles are reached.[14,29,30] However, our data show movement of the contact line during this pinning stage. This may be due to the heterogeneity of the surface. The contact line could locally reach the advancing and receding values at different times for different parts of the contact line. The contact line may therefore have some movement during the pinning phase before it reaches the stage where the advancing or receding angles are reached for the bulk of the contact line. This could occur for areas of the solid surface with different advancing and receding angles than for the rest of the liquid and also for areas of the solid surface where the local contact angle differs from the rest of the contact line. This partial pinning will be modeled computationally later in this work, but the theoretical basis remains unclear.

In addition, there is a lack of a sharp transition during the receding process. This may be explained by the difference between advancing onto an unwetted surface and receding onto a wetting one. Recent work with nanograss shows receding and advancing events can vary dramatically on micropillar surfaces.[31] This may also be true in the less extreme case of flat plates with heterogenieties. Further work is needed to investigate this behavior.

3.2. Force Analysis. The net vertical force exerted on solid surfaces by an axisymmetric capillary bridge has two components, one due to surface tension at the three-phase

contact line (F_l) and one due to the Laplace pressure inside the bridge (F_p). The total force is

$$F = F_l + F_p = 2\pi R \gamma \sin\theta - \pi R^2 \Delta P \tag{1}$$

where R is the contact radius of the liquid, θ is the contact angle, as illustrated in Figure 3, and ΔP is the Laplace pressure.
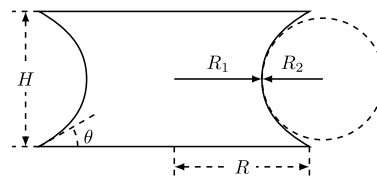
Figure 3. Geometry of the bridge. R, θ, and H are the contact radius, angle, and height of the bridge. R_1 and R_2 are the principal radii of curvature. R_1 is the neck width, and R_2 is found from fitting the bridge outline near the neck to a circle.

In this study, this force is defined as positive when the bridge causes attraction between the two solid surfaces and negative when it causes repulsion. F is averaged for all four corners to give one experimental result. The Laplace pressure is given by the Young–Laplace equation, $\Delta P = \gamma\left(\frac{1}{R_1} + \frac{1}{R_2}\right)$, where R_1 and R_2 are the principal radii of curvature. It can be approximated by fitting the bridge shape very near the midpoint to a section of a circular arc, as seen in Figure 3. Thus, R_1 is the bridge radius at the midpoint, and R_2 is the radius of the circular arc that matches the external curvature at this location. Following convention, we defined R_1 as positive and R_2 as negative for concave bridges.

Combining eq 1 and the Young–Laplace equation gives $\gamma = F/[2\pi R \sin\theta - \pi R^2(1/R_1 + 1/R_2)]$. The experimental values of F, R, θ, R_1, and R_2 at each bridge height were used to find an average γ. The resulting value, 51.1 mN m^{-1}, was 19% smaller than the published value for glycerol at room temperature, 63.4 mN m^{-1}. This suggests that the approximation for ΔP may be an overestimation.

Figure 2 shows a complicated relationship between the normal force and the bridge height. There is a nonmonotonic evolution of the force during the advancing and receding phases with smaller forces during compression and larger forces during stretching. To study this further, F_l, F_p, and F were calculated using the experimental value of γ. These quantities are plotted in Figure 4a along with the experimentally measured force. The Laplace pressure is plotted in Figure 4b.

The evolution of F_l follows that of the contact angle. This shows that the $\sin\theta$ component of F_l has a larger effect on the shape of the F_l curve than the R term. Meanwhile, the evolution of F_p shows that the $-\Delta P$ component, rather than the R^2 component, dominates the shape of the F_p curve. The radius in Figure 2 shows little change in the radius over the course of the experiment compared to the contact angle in the same figure or $-\Delta P$ in Figure 4a, which explains the limited impact of the radius on the shape of the force curves. It can also be seen that F_p has a magnitude larger than that of F_l for most bridge heights. The force from the Laplace pressure has a larger impact on the normal force than the force from the three-phase contact line.

To further investigate the evolution of the normal force, several experiments were performed at different volumes with
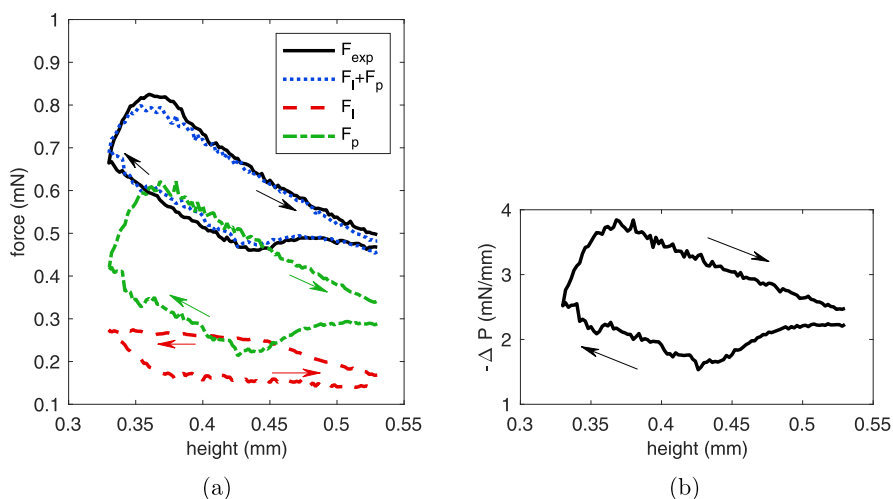
Figure 4. (a) Evolution of the force contributions to the normal force for two plates connected by a capillary bridge. Positive force measurements indicate the attraction between the plates. F_l, the force contribution due to the surface tension around the three-phase contact line, is indicated by the dash-dotted line. F_p, the force contribution due to the Laplace pressure inside the bridge, is indicated by the dashed line. The total force, $F = F_l + F_p$, is indicated by the dotted line. The experimentally measured force is indicated by a solid line. (b) Evolution of the Laplace pressure.

different starting and ending heights. They all had similar advancing and receding angles ($\theta_a \approx 60°$, $\theta_r \approx 30°$). The force progression of these experiments is shown in Figure 5. The
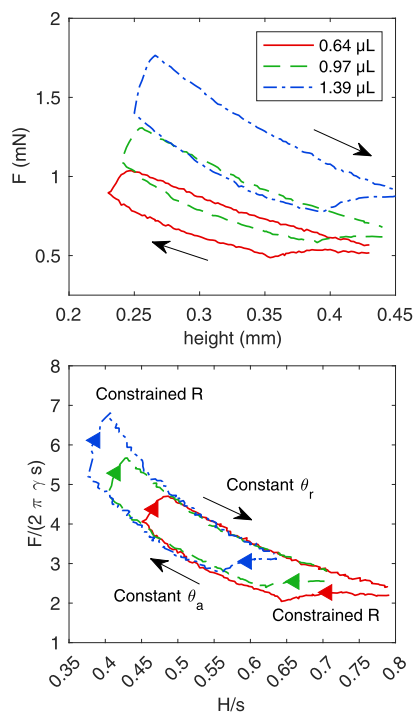
Figure 5. Force progression for three bridge experiments with different volumes and start and end heights. The bottom plot shows the normalized force progression for the same three bridge experiments. The scaling length is $s = \sqrt[3]{V/(4\pi)}$.

normal force is plotted against the height in the upper plot. The normalized force, $F/(2\pi\gamma s)$, where $s = \sqrt[3]{V/(4\pi)}$, is plotted against the normalized bridge height, H/s, in the lower plot. All the data show a similar pattern. During the initial bridge compression, there is an initial increase in the force for high normalized bridge heights, followed by a decrease as the height continues to be lowered. Once θ_a is reached there is a

steady increase in force with the decrease in bridge height. When the minimum bridge height is reached, the bridge height begins to be increased. The force increases until the receding contact angle is reached. Afterward, the force decreases as the bridge height does. The changes in increasing or decreasing force roughly correspond to stages with constrained radius or constant contact angle, as labeled in Figure 5. This same pattern has been seen in other work.[14,16]

3.3. Bridge Migration. Hysteresis can cause bridge migration between nonparallel plates. Perfectly parallel plates are expected to have the same contact angle at all positions on the contact line, but the same is not true for nonparallel plates. When there is hysteresis in the contact line motion, one location will reach θ_a or θ_r before the others, and consequently, there will be motion in the direction of the first advance of the contact line.

Consider Figure 6. All data are for the top contact line of the bridge. The top plot in Figure 6a shows the progression of the left and right contact angles. The middle plot shows the drift of the left and right edges of the contact line. The bottom plot shows the progression of the center of the contact line, X_C. Even though the angle between the top and bottom plates is < 1°, there is still visible movement of the bridge to the left, which is where the apex of the two plates is located. Points 1, 2, and 3 are illustrated by the images in Figure 6b. Between points 1 and 2, the contact angles increased toward their advancing values. Once the left contact angle reached its advancing value, the left edge of the contact line began to move outward. Meanwhile, the right contact angle had not yet reached its advancing value, and so the right edge remained stationary. This caused net movement of the contact line in the negative (left) direction, as seen in the plot of X_C in Figure 6a.

After point 2, the bridge was stretched. Both edges immediately receded. They moved a similar distance between points 2 and 3 so that the center position does not show much change. At the end of the experiment, the center had shifted toward the narrow side of the bridge. This matches previously found results for nonparallel surfaces[3,28] and indicates asymmetry in the bridge structure. The presence of this motion, despite the small angle between the plates, means that it is critical to take nonparallel bridge effects into account.
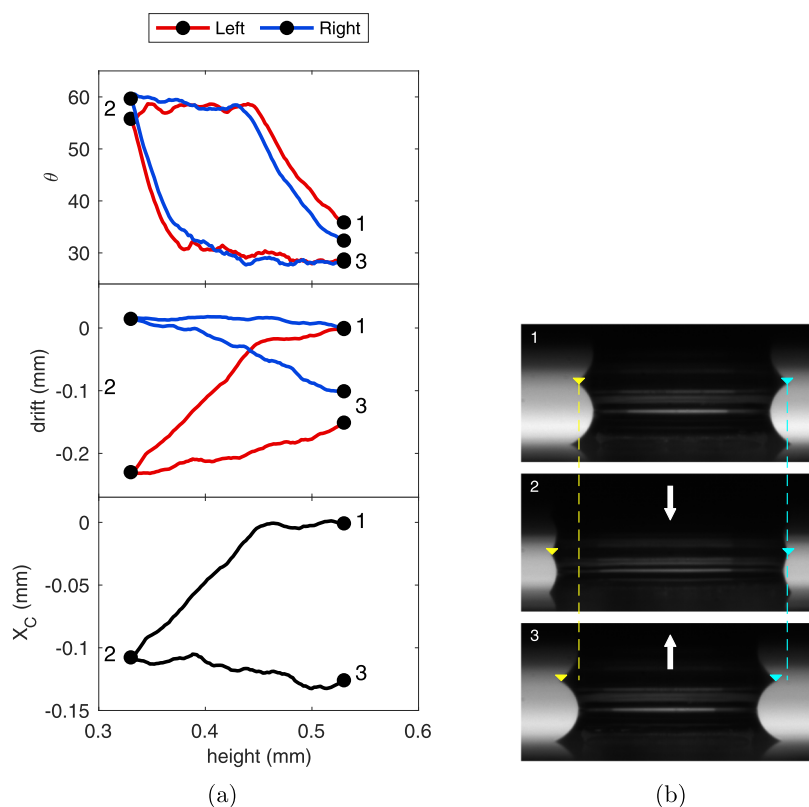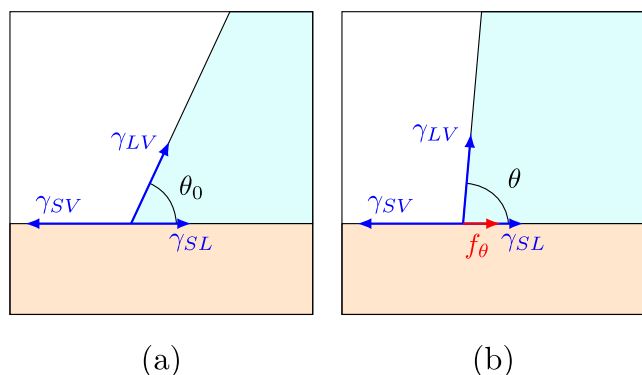
Figure 6. (a) Experimental results for the top angles and top contact line center for a capillary bridge between nonparallel plates (angle between plates is < 1°). The arrows follow the evolution of the bridge height. The top plot shows the progression of the top left and top right contact angles. The middle plot shows the drift of the top left and top right edges from their original positions. The bottom plot shows the position of the center of the top contact line, X_c. (b) Images of the evolution of a capillary bridge between nonparallel plates.

4. THEORY

4.1. Resistive Tension. In the absence of contact angle hysteresis, the angle that the bridge makes with a surface is described by Young's equation

$$\gamma \cos \theta_0 = \gamma_{SV} - \gamma_{SL} \tag{2}$$

as illustrated in Figure 7a. The liquid−vapor, solid−vapor, and solid−liquid interfacial tensions (γ, γ_{SV}, and γ_{SL}) are balanced in the direction parallel to the solid−liquid interface to find the equilibrium contact angle, θ_0. Joanny and de Gennes modeled the range of contact angles exhibited by real capillary bridges by introducing an added force per unit length, f_θ, to Young's equation.[7,17] f_θ describes the observed contact angle, θ, which is not necessarily the same as θ_0. Figure 7b shows the force balance at the contact line when f_θ is added to Young's equation model. Using Figure 7a,b, the equation for f_θ is

$$f_\theta = \gamma(\cos \theta - \cos \theta_0) \tag{3}$$

Furmidge used an energy argument to come up with a similar equation for the retention force per unit width of a droplet on an inclined surface. When a surface is wetted or dewetted by a liquid, the force per unit length is given by the modified Young-Dupré equation.[25] This force per unit length is $\gamma(1 + \cos \theta_r)$ for dewetting and $\gamma(1 + \cos \theta_a)$ for wetting. Researchers have used this to find the form of the force per unit width pinning a droplet to an inclined plane to be $F/w = \gamma k(\cos \theta_r - \cos \theta_a)$, where w is the width of the droplet perpendicular to the direction of incline, and k varies depending on the approximate geometry of the droplet. For instance, $k = 1$ if the drop has straight sides in the direction of motion[32] and $k = 4/\pi$ if a circular contact line is assumed.[33] This form also applies to drops on a spinning plate.[33]

Joanny and deGennes believed that the cause of the hysteresis was chemical and physical defects on the solid surface.[7] Tadmor presented an alternative model of drop pinning that relies on the reorientation of solid surface molecules along the triple contact line.[34] When a liquid comes in contact with a solid, the triple line creates a ridge along the solid. This causes a reorientation of the molecules along the

Figure 7. Illustration of tensions acting on the contact line. (a) Young's equation balances the liquid−vapor, solid−vapor, and solid−liquid surface tensions at the contact line. They are related by cos θ_0, the equilibrium contact angle. (b) In order to account for nonequilibrium contact angles, a new force per unit length, f_θ, is added to the Young's equation balance.

triple line where those that are more strongly attracted to the liquid stay closer to the solid surface. This will create a local energy minimum and pinning. Tadmor's equation was later altered by Xu et al.[35] The pinning force per unit length is $F/w = \frac{2w\gamma}{\pi G_s}(\cos\theta_r - \cos\theta_a)$, where G_s is the interfacial modulus, w is the drop width, and ΔP is the Laplace pressure.

The differences between these models show the complexity of the problem. The central insight is that the drop pinning force is proportional to $\gamma(\cos\theta - \cos\theta_0)$. This says nothing about the specifics of the hysteresis, but as the previous paragraphs show, it has been experimentally verified for a range of situations.

The total magnitude of the contact line force, $\tilde{F}_\theta$, is found by integrating f_θ around the contact line, i.e., ignoring the vector nature of the force. For a capillary bridge with circular radius R, this gives

$$\tilde{F}_\theta = \int_l \gamma(\cos\theta - \cos\theta_0)\mathrm{d}L$$

$$= 2\pi\gamma R(\cos\theta - \cos\theta_0) \tag{4}$$

Note that this is a global measure of the resistive tension with dimensions of force, rather than the magnitude of a force vector.

4.2. Simulation. Simulations implemented in MATLAB (MathWorks) were used to determine the shape of capillary bridges. The potential energy of the system is

$$U = U_s + U_v \tag{5}$$

where U_s is the surface energy of the liquid–vapor, solid–vapor, and solid–liquid interfaces given by $U_S = \gamma A_{LV} + \gamma_{SL}A_{SL} + \gamma_{SV}A_{SV}$ where γ and A are the surface tensions and surface areas. Using Young's equation, the surface energy can be written as $U_S = \gamma A_{LV} - \gamma\cos\theta_0 A_{SL} + C$, where $C \equiv \gamma_{SV}(A_{SV} + A_{SL})$.[36,37] Since the total solid surface area is constant, C does not contribute to the energy variations. U_v is the volume-dependent energy. The volume constraint is enforced by adding an energy penalty to change the volume V from the real volume V_0. The added energy is

$$U_v = \frac{\alpha}{2}(V - V_0)^2 \tag{6}$$

where α is a chosen compressibility coefficient. Using $\alpha = 100$ mN mm^{-3} we found volume deviations of <1%.

A dissipative "resistive force", $\tilde{F}_R$, is used to control the contact line movement. At every step of the simulation, $\tilde{F}_R$ is found using the equation

$$\tilde{F}_R = -K(R - R_0) \tag{7}$$

where R is the bridge radius and R_0 is bridge radius when $\theta = \theta_0$. K is a coefficient that controls the strength of contact line pinning. If there is complete pinning of the contact line, then K is infinite and no movement is allowed. Smaller K values allow for progressively greater contact line movement. The simulation will adjust the shape of the bridge until $\tilde{F}_\theta = \tilde{F}_R$. It is important to note that these are not two separate forces. $\tilde{F}_R$ is simply a tool used to ensure the contact line is moved in accordance to $\tilde{F}_\theta$.

To understand K consider the first cycle radius and angle curves in Figure 2. During bridge compression, the angle and bridge radius increase between $H = 0.53$ mm and $H = 0.45$ mm at which point the angle reaches its advancing value. During

bridge extension, the angle and radius decrease between $H = 0.33$ mm and $H = 0.375$ mm, and then the angle reaches its receding value. If the initial radius and angle are taken as the equilibrium values, then the final radius, R, is the radius at the beginning of the compression or extension phase, and the final angle, θ, is the advancing or receding contact angle. Since $\tilde{F}_\theta = \tilde{F}_R$, the advancing and receding resistive force coefficients, K_a and K_r, can be found using eqs 4 and 7

$$K_a = -2\pi\gamma R(\cos\theta_a - \cos\theta_0)/(R - R_0) \tag{8}$$

$$K_r = -2\pi\gamma R(\cos\theta_r - \cos\theta_0)/(R - R_0) \tag{9}$$

where R is the radius of the bridge when it reaches the advancing or receding contact angle and R_0 and θ_0 are the initial contact radius and angle.

Once K is found from the experimental data, it is used to calculate the resistive force at each simulation step. If $\theta \geq \theta_a$, then the contact angle has reached its advancing value and $\tilde{F}_R$ is set equal to $\tilde{F}_{\theta_a}$. Similarly, if $\theta \leq \theta_r$ then the contact angle has reached receding value so $\tilde{F}_R$ is set equal to $\tilde{F}_{\theta_r}$. The value of $\tilde{F}_R$ is therefore

$$\tilde{F}_R = \begin{cases} \tilde{F}_{\theta r}, & \text{if } \theta \leq \theta_r \\ -K(R - R_0), & \text{if } \theta_r < \theta < \theta_a \\ \tilde{F}_{\theta a}, & \text{if } \theta \geq \theta_a \end{cases} \tag{10}$$

with K equal to K_a while the bridge height compressed and K_r while the bridge height is stretched.

The bridge shape is defined by N vertices that are equally spaced along the y axis, as seen in Figure 8a. For height H, the
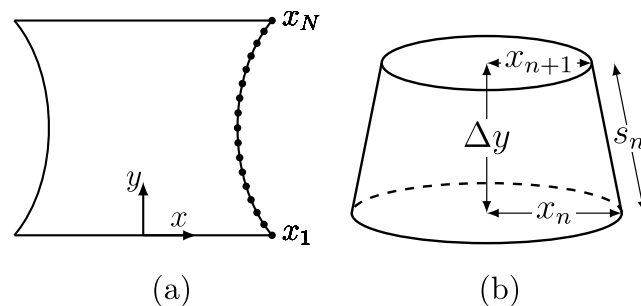
Figure 8. (a) Simulation models the bridge as a series of truncated cones with radius x_1 to x_N. x_1 is the bottom bridge radius, and x_N is the top bridge radius. At each iteration, the vertices are moved in the x direction according to the forces calculated from energy minimization. (b) A truncated cone of height Δy with bottom radius x_n, top radius x_{n+1}, and slant length s_n.
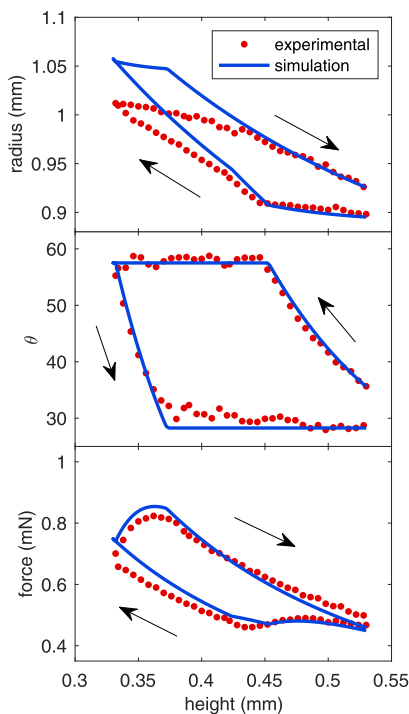
y distance between each vertex is simply $\Delta y = H/(N-1)$. The x positions of two adjacent vertices can be treated as the radii of a truncated cone like that in Figure 8b if $\Delta y \ll H$. Using only the x and y vertex positions, we are able to model the asymmetric three-dimensional bridge shape. Furthermore, since Δy is fixed for a given bridge height, only the local forces in the x direction need to be calculated.

We start the simulation by finding the radius of a cylinder with the same volume and initial height as the bridge. This radius is the starting x position for the vertices. Afterward, the gradient in the x direction of the energy in eq 5 is calculated for all vertices. The resistive force is added to this force for the two vertices at the contact line (x_1 and x_N).

The x positions are calculated through a modified velocity Verlet algorithm with damping coefficient β and time step 10^{-3}. This process is repeated until $E_k < N \times 10^{-19}$, where E_k is the sum of the velocities squared. At that point, the system is taken as having reached a steady state. The bridge height is changed in small increments and each successive bridge shape starts with the same x positions as the previous state. This is crucial for hysteresis modeling since the bridge shape is dependent on the previous shape.

The volume and initial height are easily obtained from the experimental results, but θ_0 is notoriously difficult to find for hysteretic systems. The sessile drop or the pendant drop methods have been used,[38] as well as approximations such as $\theta_0 = \frac{\theta_a + \theta_r}{2}$ or $\theta_0 = \mathrm{acos}\left(\frac{\cos\theta_a + \cos\theta_r}{2}\right)$.[29] We developed a scheme that eliminates the need to calculate the exact value of θ_0. The first simulation step is run with $\tilde{F} = 0$, $H = H_0$, the starting bridge height, and θ_0 equal to the starting experimental contact angle. The radius of the bridge formed with these parameters is our initial R_0 value. It is used for the subsequent simulation steps until the bridge height changes from increasing to decreasing or vice versa. At that point, the current θ and R are used for θ_0 and R_0.

The simulation results are plotted alongside the experimental results in Figure 9. The simulation parameters are listed in Table 1. There is a mismatch between the experimental and simulation results, especially for small bridge heights. In particular, the difference between the experimental and simulation radii at low bridge heights is about 5%. Figure 10 shows the experimental volume, as measured by using the truncated cone method, divided by the volume used for the

Table 1. Simulation Parameters

parameter (symbol)	value
top/bottom advancing angle (θ_a)	58°/52°
top/bottom receding angle (θ_r)	29°/22°
top/bottom advancing equilibrium contact angle (θ_0)	36°/25°
top/bottom receding equilibrium contact angle (θ_0)	58°/52°
top/bottom advancing resistive force coefficients (K_a)	6.51/9.67
top/bottom receding resistive force coefficients (K_r)	15.67/7.51
liquid−vapor surface tension (γ)	52.17 μN mm^{-1}
bridge volume (V_0)	1.11 μL
time step (Δt)	10^{-3} sec
compressibility coefficient (α)	100 mN mm^{-3}
damping coefficient (β)	1
number of vertices (N)	128
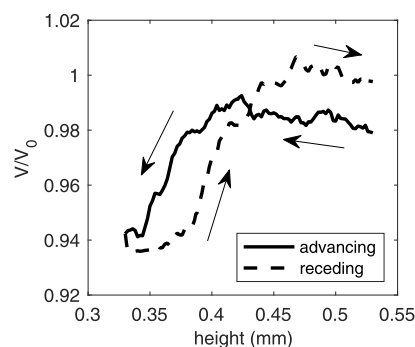
Figure 10. Experimental volume calculated using the truncated cone method divided by the simulation volume V_0. The solid line indicates an advancing contact line and the dashed line indicates a receding contact line. The dot at the beginning of the advancing stage is the start of the experiment. Arrows follow the progression of the experiment.

simulation. The experimental volume seems to decrease with bridge height. This is consistent with the solid−liquid contact area becoming noncircular due to the slanting of the top surface in the direction not measured by the camera. This is not captured by the simulation model. The volume stays within 7% of the expected value. Despite these discrepancies the simulation is able to capture the nonintuitive evolution of the force.

Figure 11 shows how $\tilde{F}_\theta$ and $\tilde{F}_R$ change with bridge height. At the beginning of the compressing phase $\tilde{F}_\theta = \tilde{F}_R = 0$. As the bridge height decreases, the θ and R increase. According to eqs

Figure 9. Experimental (solid lines) and simulation (dotted lines) results for the radius, contact angle, and normal force of a capillary bridge between two flat plates. The bridge height is lowered from 0.53 to 0.33 mm and then raised back to the original height. The arrows follow the evolution of the bridge height. Positive normal force indicates attraction between the plates.
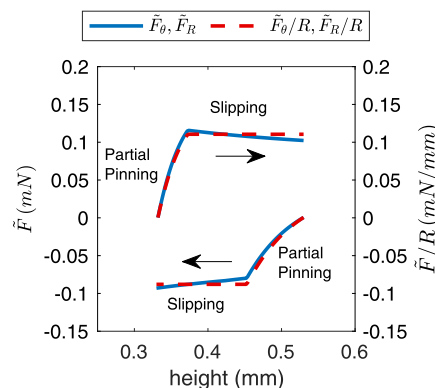

Figure 11. Resistive force and the resistive force per unit length during the simulation.

4 and 7, both $\tilde{F}_\theta$ and $\tilde{F}_R$ correspondingly decrease. Once $\theta = \theta_a$, the slipping stage begins and the force per unit length is set to $2\pi\gamma(\cos\theta_a - \cos\theta_0)$ which keeps the contact angle at the advancing value. The radius will increase much more during the slipping phase than during the partial pinning phase, but this has a small effect on the forces compared to the change of the contact angle during the partial pinning phase.

During bridge extension $\tilde{F}_\theta$ and $\tilde{F}_R$ again start at 0. θ and R decrease from their original values and $\tilde{F}_\theta$ and $\tilde{F}_R$ correspondingly increase. When θ reaches its receding value the slipping stage begins and the force per unit length is set to $2\pi\gamma(\cos\theta_r - \cos\theta_0)$. The radius will decrease dramatically during the slipping phase but again this only has a small effect on the values of $\tilde{F}_\theta$ and $\tilde{F}_R$.

5. CONCLUSIONS

Our experimental work has precisely measured the adhesive force on solid surfaces due to capillary bridges as well as the bridge shape. This has allowed us to model both hysteresis cycles, where the contact line movement is dependent on the current contact angle. Previous models only allowed movement when the advancing and receding contact angles were reached but this model introduces a force, $\tilde{F}_R$, that can be adjusted by controlling the strength of contact line pinning. We have shown that the hysteresis between nonparallel plates causes movement of the bridge center, even for very small angles.

The model does not link the resistive force constant, K, to the physical properties of the flat surfaces or the liquid. Instead it is a fitting parameter that is found from experimental data. More work needs to be done to connect the partial pinning of the contact line to the contact line force. The model also does not incorporate the tilt of the top plate. The tilt creates an elliptical rather than a circular contact line. This will need to be considered in future work.

■ AUTHOR INFORMATION

Corresponding Author

Mark D. Shattuck − *Department of Physics, The City College of New York, New York, New York 10031, United States; The City College of New York, The Benjamin Levich Institute, New York, New York 10031, United States; The City University of New York Graduate Center, Department of Physics, New York, New York 10016-4309, United States;* Email: shattuck@ccny.cuny.edu

Authors

Moyosore S. Odunsi − *The City University of New York Graduate Center, Department of Physics, New York, New York 10016-4309, United States; The City College of New York, The Benjamin Levich Institute, New York, New York 10031, United States;* orcid.org/0009-0008-7949-7959

Jeffrey F. Morris − *Department of Chemical Engineering, The City College of New York, New York, New York 10031, United States; The City College of New York, The Benjamin Levich Institute, New York, New York 10031, United States;* orcid.org/0000-0002-0464-8846

Complete contact information is available at: https://pubs.acs.org/10.1021/acs.langmuir.3c01550

Notes

The authors declare no competing financial interest.

■ ACKNOWLEDGMENTS

■ REFERENCES

(1) Kholodov, V. A.; Yaroslavtseva, N. V.; Yashin, M. A.; Frid, A. S.; Lazarev, V. I.; Tyugai, Z. N.; Milanovskiy, E. Y. Contact angles of wetting and water stability of soil structure. *Eurasian Soil Sci.* 2015, 48, 600−607.
(2) de Gans, B. J.; Duineveld, P. C.; Schubert, U. Inkjet Printing of Polymers: State of the Art and Future Developments. *Adv. Mater.* 2004, 16, 203−213.
(3) Prakash, M.; Quéré, D.; Bush, J. W. M. Surface Tension Transport of Prey by Feeding Shorebirds: The Capillary Ratchet. *Science* 2008, 320, 931−934.
(4) Piner, R. D.; Mirkin, C. A. Effect of Water on Lateral Force Microscopy in Air. *Langmuir* 1997, 13, 6864−6868.
(5) Young, T. An essay on the cohesion of fluids. *Philos. Trans. R. Soc. London* 1805, 95, 65−87.
(6) Drelich, J. W. Contact angles: From past mistakes to new developments through liquid-solid adhesion measurements. *Adv. Colloid Interface Sci.* 2019, 267, 1−14.
(7) Joanny, J. F.; de Gennes, P. G. A model for contact angle hysteresis. *J. Chem. Phys.* 1984, 81, 552−562.
(8) Fortes, M. Axisymmetric liquid bridges between parallel plates. *J. Colloid Interface Sci.* 1982, 88, 338−352.
(9) de Gennes, P. G. Wetting: statics and dynamics. *Rev. Mod. Phys.* 1985, 57, 827−863.
(10) Shi, Z.; Zhang, Y.; Liu, M.; Hanaor, D. A.; Gan, Y. Dynamic contact angle hysteresis in liquid bridges. *Colloids Surf., A* 2018, 555, 365−371.
(11) Huang, C.-H.; Carvalho, M. S.; Kumar, S. Stretching liquid bridges with moving contact lines: comparison of liquid-transfer predictions and experiments. *Soft Matter* 2016, 12, 7457−7469.
(12) Kumar, S. Liquid transfer in printing processes: Liquid bridges with moving contact lines. *Annu. Rev. Fluid. Mech.* 2015, 47, 67−94.
(13) Nagy, N. Contact angle determination on hydrophilic and superhydrophilic surfaces by using r−θ-type capillary bridges. *Langmuir* 2019, 35, 5202−5212.
(14) Chen, H.; Amirfazli, A.; Tang, T. Modeling Liquid Bridge between Surfaces with Contact Angle Hysteresis. *Langmuir* 2013, 29, 3310−3319.
(15) De Souza, E. J.; Gao, L.; McCarthy, T. J.; Arzt, E.; Crosby, A. J. Effect of Contact Angle Hysteresis on the Measurement of Capillary Forces. *Langmuir* 2008, 24, 1391−1396.
(16) Moghadam, A.; Vahedi Tafreshi, H. On liquid bridge adhesion to fibrous surfaces under normal and shear forces. *Colloids Surf., A* 2020, 589, 124473.
(17) Adam, N. K.; Jessop, G. CCL. Angles of contact and polarity of solid surfaces. *J. Chem. Soc., Trans.* 1925, 127, 1863−1868.
(18) Lee, E.; Müller-Plathe, F. Effect of Polymer on the Contact Line Friction of a Capillary Bridge. *Macromolecules* 2022, 55, 2649−2658.
(19) Mastrangeli, M.; Valsamis, J.-B.; Van Hoof, C.; Celis, J.-P.; Lambert, P. Lateral capillary forces of cylindrical fluid menisci: a comprehensive quasi-static study. *J. Manuf. Syst.* 2010, 20, 075041.
(20) Wiklund, H. S.; Uesaka, T. Simulations of shearing of capillary bridges. *J. Chem. Phys.* 2012, 136, 094703.
(21) Song, Q.; Liu, K.; Sun, W.; Chen, R.; Ji, J.; Jiao, Y.; Gao, T.; Ye, J. Lateral and Normal Capillary Force Evolution of a Reciprocating Liquid Bridge. *Langmuir* 2021, 37, 11737−11749.
(22) Barrio-Zhang, H.; Ruiz-Gutiérrez, É.; Armstrong, S.; McHale, G.; Wells, G. G.; Ledesma-Aguilar, R. Contact-Angle Hysteresis and Contact-Line Friction on Slippery Liquid-like Surfaces. *Langmuir* 2020, 36, 15094−15101.

(23) Pierce, E.; Carmona, F.; Amirfazli, A. Understanding of sliding and contact angle results in tilted plate experiments. *Colloids Surf., A* **2008**, *323*, 73−82.

(24) Gao, N.; Geyer, F.; Pilat, D.; Wooh, S.; Vollmer, D.; Butt, H.; Berger, R. How drops start sliding over solid surfaces. *Nat. Phys.* **2018**, *14*, 191−196.

(25) Furmidge, C. Studies at phase interfaces. I. The sliding of liquid drops on solid surfaces and a theory for spray retention. *J. Colloid Sci.* **1962**, *17*, 309−324.

(26) Wang, Y.; Zhao, J.; Zhang, D.; Jian, M.; Liu, H.; Zhang, X. Droplet Sliding: The Numerical Observation of Multiple Contact Angle Hysteresis. *Langmuir* **2019**, *35*, 9970−9978.

(27) Luo, C.; Heng, X.; Xiang, M. Behavior of a Liquid Drop between Two Nonparallel Plates. *Langmuir* **2014**, *30*, 8373−8380.

(28) Ataei, M.; Tang, T.; Amirfazli, A. Motion of a liquid bridge between nonparallel surfaces. *J. Colloid Interface Sci.* **2017**, *492*, 218−228.

(29) Santos, M. J.; White, J. A. Theory and Simulation of Angular Hysteresis on Planar Surfaces. *Langmuir* **2011**, *27*, 14868−14875.

(30) Athukorallage, B.; Aulisa, E.; Iyer, R.; Zhang, L. Macroscopic Theory for Capillary-Pressure Hysteresis. *Langmuir* **2015**, *31*, 2390−2397.

(31) Vieira, A.; Cui, W.; Jokinen, V.; Ras, R. H.; Zhou, Q. Through-drop imaging of moving contact lines and contact areas on opaque water-repellent surfaces. *Soft Matter* **2023**, *19*, 2350−2359.

(32) Dussan V, E. B.; Chow, R. T. P. On the ability of drops or bubbles to stick to non-horizontal surfaces of solids. *J. Fluid Mech.* **1983**, *137*, 1−29.

(33) Extrand, C.; Gent, A. Retention of liquid drops by solid surfaces. *J. Colloid Interface Sci.* **1990**, *138*, 431−442.

(34) Tadmor, R. Open problems in wetting phenomena: pinning retention forces. *Langmuir* **2021**, *37*, 6357−6372.

(35) Xu, W.; Xu, J.; Li, X.; Tian, Y.; Choi, C.-H.; Yang, E.-H. Lateral actuation of an organic droplet on conjugated polymer electrodes via imbalanced interfacial tensions. *Soft Matter* **2016**, *12*, 6902−6909.

(36) Miot, M.; Veylon, G.; Wautier, A.; Philippe, P.; Nicot, F.; Jamin, F. Numerical analysis of capillary bridges and coalescence in a triplet of spheres. *Granular Matter* **2021**, *23*, 65.

(37) Brandon, S.; Wachs, A.; Marmur, A. Simulated contact angle hysteresis of a three-dimensional drop on a chemically heterogeneous surface: a numerical example. *J. Colloid Interface Sci.* **1997**, *191*, 110−116.

(38) Gennes, P.-G.; Brochard-Wyart, F.; Quéré, D. *Capillarity and Wetting Phenomena*; Springer: New York, NY, 2004.